Article:
Von den Driesch, N, Stange, D, Wirths, S et al. (11 more authors) (2017) SiGeSn Ternaries for Efficient Group IV Heterostructure Light Emitters. Small, 13 (16). 1603321. ISSN 1613-6810

https://doi.org/10.1002/smll.201603321

DOI: 10.1002/ ((please add manuscript number))
Article type: Full Paper

SiGeSn Ternaries for Efficient Group IV Heterostructure Light Emitters

Nils von den Driesch, Daniela Stange, Stephan Wirths, Denis Rainko, Ivan Povstugar, Aleksei Savenko, Uwe Breuer, Richard Geiger, Hans Sigg, Zoran Ikonic, Jean-Michel Hartmann, Detlev Grützmacher, Siegfried Mantl, and Dan M. Buca**

N. von den Driesch, D. Stange, Dr. S. Wirths, D. Rainko, Prof. D. Grützmacher, Prof. S. Mantl, Dr. D. M. Buca
Peter Grünberg Institute 9 (PGI-9) and JARA-Fundamentals of Future Information Technologies (JARA-FIT), Forschungszentrum Juelich, 52425 Juelich, Germany
E-mail: n.von.den.driesch@fz-juelich.de, d.m.buca@fz-juelich.de

Dr. I. Povstugar, Dr. A. Savenko, Dr. U. Breuer
Central Institute for Engineering, Electronics and Analytics – Analytics, Forschungszentrum Juelich, 52425 Juelich, Germany

Dr. R. Geiger, Dr. H. Sigg
Laboratory for Micro- and Nanotechnology (LMN), Paul Scherrer Institute, CH-5232 Villigen, Switzerland.

Dr. Z. Ikonic
Institute of Microwaves and Photonics, School of Electronic and Electrical Engineering, University of Leeds, Leeds LS2 9JT, United Kingdom

Dr. J.-M. Hartmann
CEA, LETI, MINATEC Campus, F-38054 Grenoble, France
Univ. Grenoble Alpes, F-38000 Grenoble, France

Keywords: SiGeSn, group IV, heterostructures, light emitting diodes, silicon photonics

SiGeSn ternaries were grown on Ge-buffered Si wafers incorporating Si or Sn contents of up to 15 at.%. The ternaries exhibit layer thicknesses up to 600 nm, while maintaining a high crystalline quality. Tuning of stoichiometry and strain, as shown by means of absorption measurements, allows bandgap engineering in the short-wave infrared (SWIR) range of up to about 2.6 µm. Temperature-dependent photoluminescence (PL) experiments indicate ternaries near the indirect-to-direct bandgap transition, proving their potential for ternary-based light emitters in the aforementioned optical range. The ternaries' layer relaxation was also monitored, to explore their use as strain-relaxed buffers (SRB), since they are of interest not only for light

emitting diodes investigated in this paper, but also for many other optoelectronic and electronic applications. In particular, we have epitaxially grown a GeSn/SiGeSn multi quantum well (MQW) heterostructure, which employs SiGeSn as barrier material to efficiently confine carriers in GeSn wells. Strong room temperature light emission from fabricated light emitting diodes proves the high potential of this heterostructure approach.

1. Introduction

Merging the successful Si technology with photonic systems promises a dramatically reduced power consumption for future IC electronics. In particular, silicon (Si) photonics, due to its excellent compatibility with Si complementary metal oxide semiconductor (CMOS) technology, is the prime candidate for realizing electronic photonic integrated circuits (EPICs)[1,2]. Many optoelectronic components, such as photodetectors[3], photonic bandgap optical fibers[4], optical modulators[5] or even electronic-photonic systems, integrating hundreds of passive photonic components with state-of-the-art electronics[6], are already available based on group IV semiconductors. While integration of III-V materials show promising results[7,8], a Si-based efficient electrically pumped light source would be the final missing ingredient for the fabrication of all included EPICs on this platform. To overcome the obstacle of the indirect bandgap in elemental Si or Ge, substitutional incorporation of Sn into the Ge lattice has been investigated both theoretically[9–11] and experimentally[12–14]. Recent advances in both Sn incorporation and strain engineering has led to the proof of fundamental direct bandgap in GeSn binary alloys[15,16], as well as the demonstration of lasing at low temperatures.[16,17]

Present research on Si-compatible light emitters is based on the above mentioned breakthroughs, including the investigation of heterostructures, such as double heterostructures[18] (DHS) or multi quantum wells[19] (MQW), suitable for carrier confinement in GeSn active optical material. A natural candidate material for claddings or barriers in DHS or MQW, are group IV ternary SiGeSn alloys[20,21]. Compared to GeSn, the additional degree of freedom offered by the

introduction of Si allows independent tuning of lattice constant and bandgap energy[22]. In particular, appropriate combinations of Si and Sn contents, together with strain engineering, will yield SiGeSn ternary alloys with a direct bandgap[1]. Driven by photonic applications, strong efforts have been made investigating the epitaxial growth of SiGeSn alloys in recent years[23–25]. A multitude of applications of this material in nanoelectronic[26], optoelectronic[27] or photovoltaic applications [28] is foreseen.

Despite the large potential of these materials, such ternaries still pose many challenges, both in fabrication and theoretical. One of the main difficulties concerning epitaxy and processing of Sn-containing group IV alloys arises from their poor thermodynamic stability. The low (< 1 at.%) solid solubility of Sn in Ge[29] requires the use of very low growth temperatures (below about 400°C[12]), limiting the thermal budget for future device processing[30]. However, the incorporation of Si atoms in GeSn to form ternaries is believed to enhance thermal stability, making them more robust and suitable for device applications, compared to their binary counterparts[31]. From a theoretical point of view, calculation of SiGeSn band structures and alignments relies, amongst others, on bowing parameters for direct and indirect bandgaps, with a wide variation of values reported in different studies[32,33].

In this contribution, we present the epitaxial growth and optical properties of SiGeSn alloys with Si and Sn concentrations both up to about 14 at.%, aiming for electrically-driven light emitting devices. The crystalline quality of the epitaxial layers is confirmed by techniques such as Rutherford Backscattering Spectrometry (RBS) or cross-sectional Transmission Electron Microscopy (XTEM). Tailoring Si and Sn concentration in the alloy enables band structure engineering, leading to light absorption and emission energy tunability from ~0.5 eV (as in the demonstrated GeSn laser in Ref. [16]) up to ~0.8 eV (like elemental Ge emission), as indicated by photoluminescence (PL) and reflectance measurements, respectively. Strain relaxation in ternaries, as evidenced by X-ray diffraction (XRD), allows their use as strain relaxed buffers (SRB) to tune the stress in subsequently grown device heterostructures, in order to improve the

Γ-L valley separation. Finally, we combine SiGeSn ternaries with active GeSn layers to epitaxially grow GeSn/SiGeSn MQW LEDs and investigate their structural and light emitting properties.

2. Results

2.1. Film growth and layer strain relaxation

The growth temperature dependence of Si and Sn incorporation was studied on coherently grown ternaries on Ge-VS. For fixed partial pressures of $p(Ge_2H_6)$ = 54 Pa, $p(Si_2H_6)$ = 68 Pa and $p(SnCl_4)$ = 0.6 Pa, a strong opposite dependency of Si and Sn incorporation on growth temperature is observed, as shown in **Figure 1**(a). Similar to the epitaxy of binary GeSn alloys[12], a strong increase of Sn concentration, ranging from 5 at.% up to 12 at.% is observed when the growth temperature is lowered from 425°C down to 340°C. One explanation for such behavior originates from temperature-induced reduction of the Sn segregation length[34]. Epitaxy of alloys well above the equilibrium solubility limit leads to phase separation via out-diffusion of Sn from the layer. However, diffusion can be effectively suppressed by temperature reduction, as long as high growth rates (ranging between 10-50 nm min^{-1} at 340-400°C) are provided.

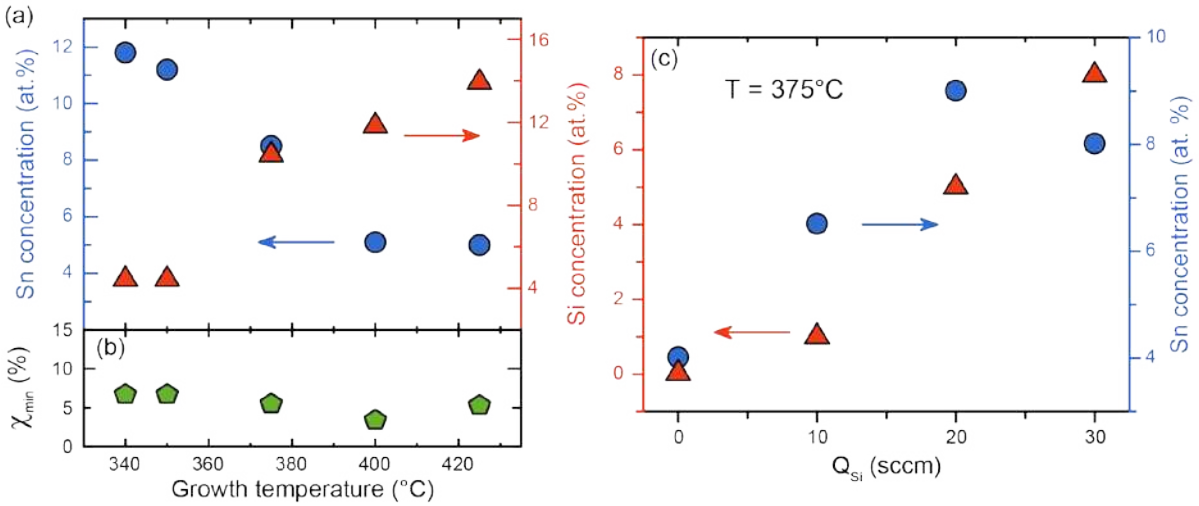

Figure 1. *Si (orange triangles) and Sn (blue circles) concentrations (a) and minimum channeling yield dependence (b) on growth temperature for constant precursor flows. (c): Si and Sn incorporation at 375°C for variable disilane flows.*

A reverse incorporation effect, an increase at elevated temperatures, is observed for Si atoms. This behavior can be understood considering the binding energies of the different precursors, 3.20 eV[35] for disilane, compared to 2.87 eV[35] for digermane. Therefore, the Si precursor's cracking efficiency is much stronger impaired at lower temperatures and the resulting smaller number of SiH_x radicals on the wafer surface ultimately leads to a decreased number of incorporated Si atoms in the lattice. Additionally, surface reactions may play an important role during epilayer growth. Complex chemical reactions on the wafer surface between the hydride radicals and the chlorine-containing Sn precursor, not yet fully understood, may supply additional heat, allowing Si incorporation at such low temperatures in the first place. Thus, slight parameter variations can lead to strong changes in surface kinetics and, therefore, in the resulting layer properties. This behavior can also be observed by tuning the supply of disilane during growth at constant growth temperature. Starting from binary GeSn, increasing the disilane flow up to 30 sccm raises the Si incorporation to about 8 at.%, as illustrated in Figure 1(c). At the same time, the Sn concentration is lifted, here from 4 to about 8 at.%, as previously observed in SiGeSn epitaxy[24].

Regardless of growth conditions, all epitaxial SiGeSn layers show a very high atom substitutionality, as indicated in Figure 1(b). A very small minimum channeling yield χ_{min} below 7 % is obtained for all samples. Therefore, we may conclude that even for highest Sn concentrations (low growth temperatures), and for highest Si contents (high growth temperatures), the Sn atoms do not occupy interstitial sites or form precipitates in the bulk.

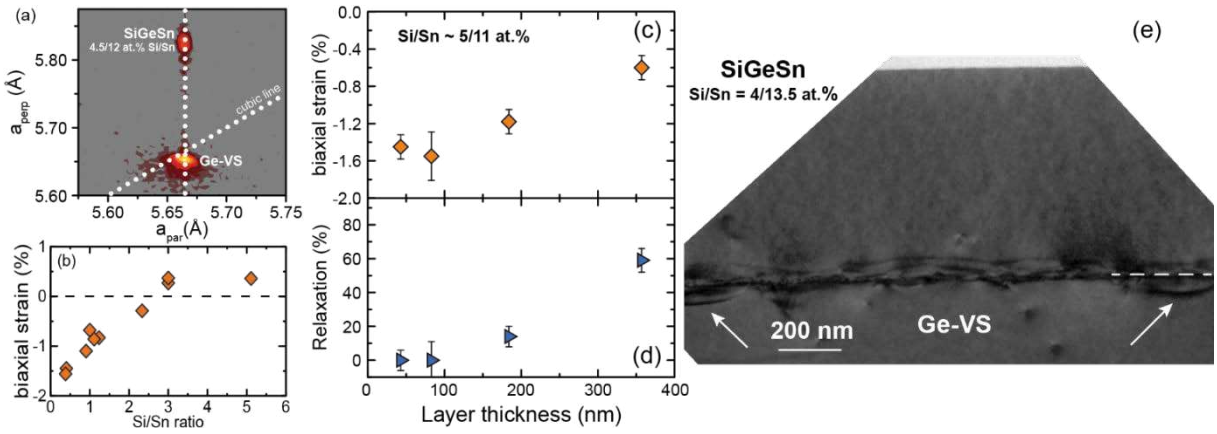

Figure 2. *(a): Reciprocal space map of pseudomorphically grown $Si_{0.045}Ge_{0.837}Sn_{0.118}$. (b): Strain dependence of coherently grown ternaries on their Si/Sn ratio. (c)/(d): Biaxial strain and degree of relaxation evolution in ternaries with increasing layer thickness. (e): Cross-sectional TEM micrograph of a 600 nm thick SiGeSn alloy.*

The built-in biaxial strain in layers grown on Ge-VS was precisely determined (±0.1 %) employing reciprocal space mapping. An exemplary diffractogram for a ternary with Si/Sn concentration of 4.5/12 at.% with a thickness of 48 nm is shown in **Figure 2**(a). The diffraction peak is positioned well above the cubic line at a larger perpendicular than in-plane lattice constant, indicating compressive strain. Additionally, the in-plane lattice constant matches that of the Ge-VS, proving pseudomorphic growth on the Ge-VS buffer. Apart from that, slight oscillations around the SiGeSn peak along the pseudomorphic line can be observed, indicating a smooth surface and flat SiGeSn/Ge-VS interface.

Tuning the Si/Sn ratio in the ternary, e.g. by varying the growth temperature, enables a wide tuning range of biaxial strain in the alloy. Large biaxial compressive strains of about -1.56 % are measured for small Si/Sn ratios, such as the one shown in Figure 2(a). Reducing the amount of Sn and/or increasing the amount of Si in the ternary leads to a reduction of the compressive strain until at about 12/4 at.% Si/Sn incorporation, where the grown alloy is nearly lattice matched to the underlying Ge-VS. Increasing the Si/Sn ratio even more induces a slight tensile strain in the layer, as depicted in Figure 2(b).

To further investigate strain relaxation in the ternaries, a set of samples was grown using nominally the same recipe with only differing growth times, leading to ternaries with a Si/Sn incorporation of about 5/11 at.% and varying thicknesses up to about 360 nm. Figure 2(c) depicts that the two layers with thicknesses up to about 85 nm are still fully strained on the Ge-VS. Compressive strain values of about -1.50 %, consistent within measurement errors, have been obtained in those samples. Plastic strain relaxation via dislocations formation, energetically favorable in layers grown above the critical thickness, leads to a degree of strain relaxation of about 60 % in a 360 nm thick layer, as can be seen in Figure 2(d)

Strain relaxation in the alloy is promoted by the formation of a dense misfit dislocation network close to the SiGeSn/Ge-VS interface, as exemplified by the XTEM micrograph of a 600 nm thick SiGeSn layer with 4/13.5 at.% Si/Sn shown in Figure 2(e). Several dislocation half-loops, connecting the ends of strain-relieving misfit segments formed at the interface, are observed to penetrate into the Ge-VS (marked by white arrows in Figure 2(e)). A similar behavior, in which the buffer actively participates in the strain relaxation mechanism, has already been noticed for GeSn binaries grown at low temperatures on Ge-VS in the same reactor[12]. The absence of extended defects in the SiGeSn layer, like threading dislocations or stacking faults, is especially beneficial for opto- and nanoelectronic applications, since e.g. threading dislocations are known to form midgap trap states[36], thus seriously influencing device performance.

2.2. Optical Characterization

The influence of both, the alloy composition as well as compressive strain, on electronic band structure can be quantified by investigating the change of absorption and emission properties. The position of the strong absorption edge, associated with the direct bandgap in the material, is evidenced by spectral reflectometry. Three sets of SiGeSn alloys are presented here and given in **Table 1**: i) with a fixed Sn concentration of about 5 at.% and various Si contents (**Figure 3**(a)); ii) with a constant Si content of ~4.5% and various Sn contents (Figure 3(b)); iii) with constant composition, but different strain states (Figure 3(c)).

Table 1. Sample overview of the different series, investigated by optical measurements.

Sample series	Si composition [at.%]	Sn composition [at.%]	layer thickness [nm]	strain [%]
Constant Sn incorporation	5.0	5.0	50	-0.39
	11.9	5.1	67	-0.29
	15.0	5.0	90	0.27
Constant Si incorporation	5.0	5.0	50	-0.39
	4.5	11.8	48	-1.56
	4.5	13.5	598	-0.59
Constant stoichiometry	4.5	11.2	43	-1.50
	5.5	10.5	184	-1.18
	4.5	11.5	357	-0.60
PL series	12.0	4.0	200	0.37
	6.0	11.0	195	-0.75
	4.0	13.0	243	-0.64

In the first case, the reflection spectra show only a strong absorption edge near 0.80 eV, same as for the underlying Ge-VS. In these thin layers, especially with high Si contents, the direct bandgap is close to or above the value of the Ge-VS bandgap, thus reflection measurements for samples mounted on top of a reflective holder are limited by absorption from the Ge buffer having the smallest gap. For the second case of a low and constant Si content and a Sn concentration which increases from 5 at.% up to 11.8 at.% in coherently grown samples, a distinct shift of the absorption edge is observed. This shift is related to bandgap lowering, caused by the increasing incorporation of Sn atoms. The position of the absorption edge is, however, also influenced by compressive strain in the layer, which blueshifts the bandgap. This has to be considered for example for the ternary alloy with Si/Sn incorporation of 4.5/13.5 at.% (blue line in Fig 3(b)), which is partially strain relaxed with a residual compressive strain of about -0.59 %, while the lower Sn content alloys are grown pseudomorphically on the Ge-VS.

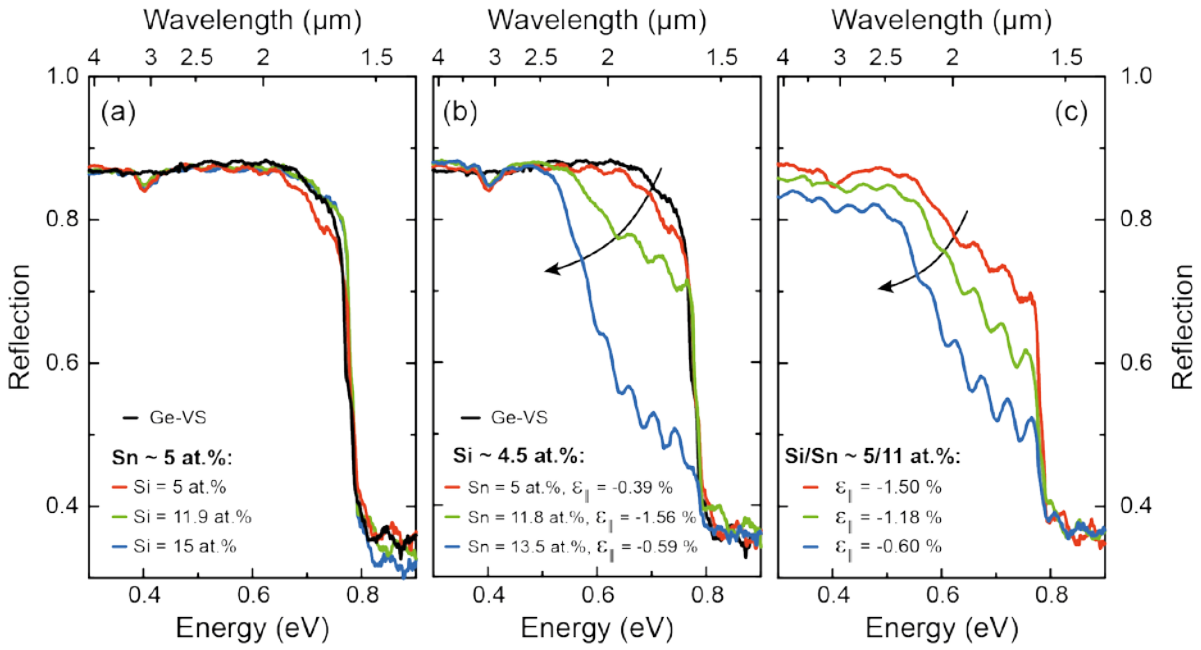

Figure 3. *Reflection measurements on SiGeSn ternaries with different stoichiometries. (a): Sample series with constant Sn and (b) constant Si concentrations. (c): Evolution of reflection for* $Si_{0.05}GeSn_{0.11}$ *layers under varying compressive strains.*

For a clearer observation of the influence of strain relaxation on the optical properties, reflectance spectra on the thickness series (see Figure 2(c/d)) were acquired and shown in Figure 3(c). Light absorption, at smaller energies and thus not related to the Ge-VS, is redshifted to higher wavelengths as the compressive strain decreases. From a Tauc plot, a decline of the direct bandgap transition from 0.61 eV to 0.55 eV is observed, when the compressive strain diminishes from -1.50 % to -0.60 %.

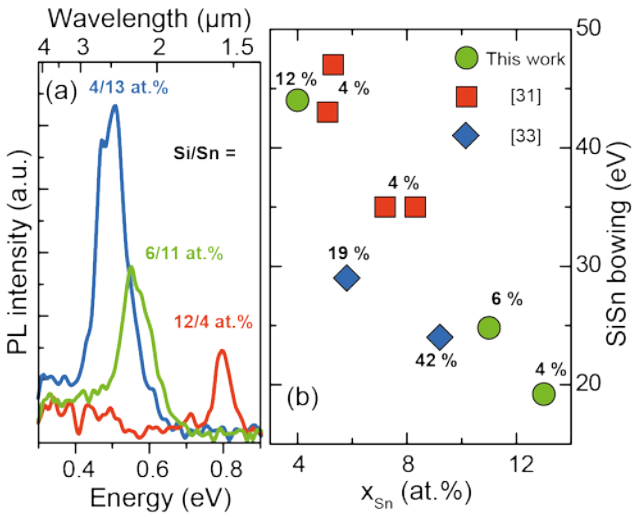

Figure 4. *(a): Composition dependent shift of PL emission of SiGeSn ternaries. (b): SiSn bowing parameters, which deliver the best fit to the PL data from a) and their comparison with literature data. A composition dependence (Si content is given next to data points) is indicated by the results.*

As discussed in the introduction, band structure calculations require the knowledge of the binaries' bowing parameters, for example, for precise determination of the Γ–valley position:

$$E_\Gamma = E_\Gamma^{Si}x + E_\Gamma^{Ge}y + E_\Gamma^{Sn}z - b^{SiGe}xy - b^{GeSn}yz - b^{SiSn}xz, \quad (1)$$

where x/y/z denote the Si/Ge/Sn concentrations (and $y = 1 - x - z$), $E_\Gamma^{Si/Ge/Sn}$ the Γ-valley of single elements and b the bowing parameter for the binaries. While bowing parameters b for SiGe and GeSn are quite well agreed on in the literature, values for b^{SiSn} strongly diverge, between 2 eV, based on ellipsometry[37] and 29 eV, determined by photoluminescence[33].

Here, we report on room temperature PL emission for three SiGeSn alloys with different stoichiometry and comparable thicknesses of about 200 nm, depicted in **Figure 4**(a). Details on the samples can be also found in Table 1. Light emission is attributed to direct band-to-band recombination at the Γ-valley between conduction band and top valence band, which can be either a heavy- or light-hole band, depending on the exact strain (and, in turn, on the sample stoichiometry). For the Si rich alloy with Si and Sn concentrations of 12 and 4 at.%, respectively,

the PL peak position is at about 0.8 eV, which shifts for a Sn rich ternary with 6/11 at.% to 0.55 eV. For even higher/smaller amounts of Sn/Si, PL emission is further shifted into the infrared at 0.49 eV, equivalent to a wavelength of 2.53 μm. Additionally, PL intensity is strongly enhanced compared to the other samples of lower Sn content. This boost in light emission is attributed to a reduced energy difference between indirect L- and direct Γ- conduction band valleys for the higher Sn content ternary. Though still being a fundamental indirect semiconductor, the smaller/larger Si/Sn incorporation leads to a downward shift of the Γ- compared to the L-valley. Therefore, a larger fraction of electrons can be excited in the direct valley, allowing efficient radiative transitions. Additionally, as in GeSn binaries, residual compressive strain, coming naturally from growth on Ge-VS, also decreases the directness of the ternary, strongly deteriorating light emission efficiency. Avoiding compressive strain in the grown layers is therefore of great importance, when tailoring SiGeSn alloys for optoelectronic applications.

By fitting the PL peaks from Figure 4(a) using eq. 1 (with additional strain correction) only by variation of b^{SiSn}, we could not find a single b^{SiSn} value, satisfactory for all samples. As shown in Figure 4(b), the obtained values spread strongly between 19 eV for the Sn rich and 44 eV for the Si rich ternary. These findings, which are in line with the spread in literature, confirm that a single, constant bowing parameter cannot be valid over the whole SiGeSn alloy range, but should either be made composition dependent, or alternatively a number of higher-order (cubic) terms may have to be added to Eq.(1). Similar compositional dependence of the direct bandgap was found for example also in InGaN [38] or GaSbN [39] ternaries. In Figure 4(b) we also included b^{SiSn}, extracted from Ref. [31] and [33]. Comparing samples with a low and constant Si content, a clear decline of b^{SiSn} with increasing Sn concentration can be observed. On the other hand, the available data are not yet sufficient to draw a clear conclusion on the magnitude of the bowing parameter for constant Sn, but variable Si concentrations. Relying on the available data,

we choose a b^{SiSn} value of 19.2 eV for bandstructure calculation of high Sn content ternaries in the following.

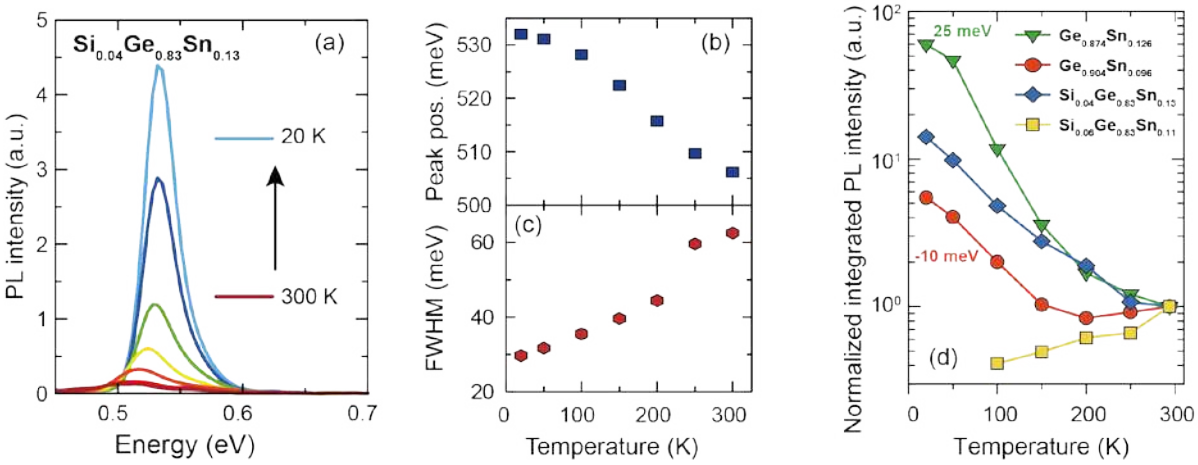

Figure 5. *(a): Temperature dependent photoluminescence spectra of a $Si_{0.04}Ge_{0.83}Sn_{0.13}$ sample and associated shifts in peak position (b) and FWHM (c). (d): Comparison of the normalized integrated PL intensity of two GeSn binaries (Γ-L valley difference given next to data) and two SiGeSn ternaries indicate a ternary (blue) at the indirect-to-direct bandgap transition.*

Temperature dependent PL spectra of a partially relaxed ternary with 4/13 at.% Si/Sn (see **Figure 5**(a)) reveal a strong emission increase, when cooling it from room temperature down to 20 K. The shift of the PL peak position in Figure 5(b) shows a Varshni-like behavior, i.e. a distinct quadratic shrinking at elevated temperatures. On the other hand, the FWHM, depicted in Figure 5(c), increases at raised temperatures, in agreement with temperature dependent broadening of the carrier distribution. The strong emission increase itself can be explained by a combination of conduction band valley occupation and changes in non-radiative recombination time. When lowering temperature, carriers condense into the lowest available conduction band state at Γ or L, depending on the exact band alignment in the SiGeSn alloy, increasing or decreasing luminescence efficiency. Suppression of non-radiative recombination paths at cryogenic temperatures leads to an additional emission enhancement. This behavior is

exemplified in Fig 5(d), comparing the integrated PL emission of two ternaries with those of two previously investigated binaries[16]. Fitting a joint density of states (JDOS) model, differences between L and Γ-valley of 25 meV and -10 meV were obtained for 12.6 at.% and 9.6 at.% GeSn samples, respectively. The SiGeSn sample with 6/11 at.% Si/Sn shows only a continuous PL decline, vanishing below 100 K, characteristic for indirect bandgap semiconductors[16]. On the other hand, the integrated intensity trend for the ternary alloy with 4/13 at.% Si/Sn lies exactly in between those of the two GeSn binaries. Assuming the same parameters as for GeSn, the JDOS model yields a valley difference of 10 meV for this sample. However, deviations in the low-temperature regime indicate different non-radiative recombination times, which has to be clarified by additional data. Nevertheless, bandstructure calculations using $b^{SiSn} = 19.2\ eV$ (see Figure 4(b)) also predict a direct bandgap semiconductor, however, with a Γ-valley about 40 meV below the L-valley, apparently overestimating the directness of the alloy. The prospect of a direct bandgap SiGeSn alloy demonstrates the possibility of ternary-based group IV light emitters, also allowing the extension of the available optical range to shorter wavelengths in the infrared range.

2.3. MQW heterostructure light emitters

By combining all important components, we subsequently demonstrate the potential of those SiGeSn ternaries by implementing them in a more advanced growth scheme for light emitting diodes. From previous theoretical and experimental findings, bulk germanium is known to provide only small band discontinuities in GeSn/Ge multi quantum well diodes[19]. SiGeSn (instead of Ge) was proposed as a more ideal barrier material in such light emitters, however, no experimental proof is available to date in literature. We have, therefore, implemented SiGeSn as barrier material, embedding GeSn active layers, to favor efficient light emission in the resulting device.

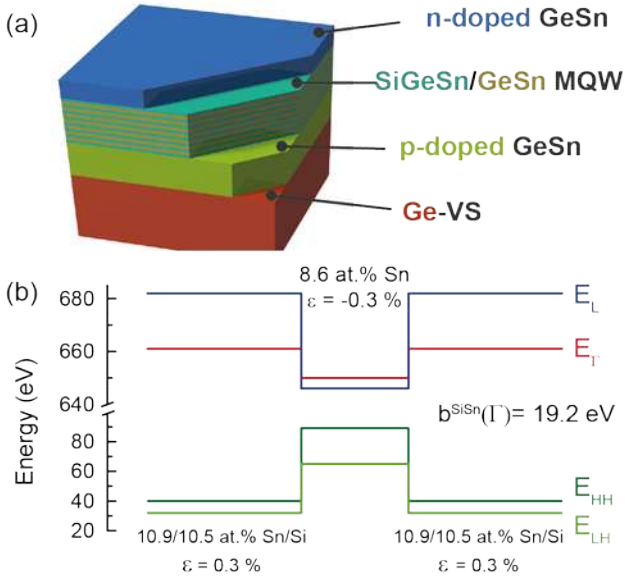

Figure 6. *(a): Schematic overview on the grown MQW heterostructure. (b): Bandstructure calculations show the carrier confinement of both electrons and holes in the active well region.*

A schematic overview on the grown heterostructure is shown in **Figure 6** (a). The MQW is grown on top of about 280 nm n-type doped GeSn (active electron concentration of 4E19 cm^{-3}).The binary with Sn content of 8.6 at.% acts as a partially strain-relaxed buffer to increase the directness of the active layers on top. Strain-relaxation in the GeSn buffer occurs via misfit dislocations at the interface with the Ge-VS. However, given the rather large buffer thickness, those defects, which may introduce additional non-radiative recombination paths, are well separated from the MQW active region. The GeSn/SiGeSn MQW on top consists of seven GeSn wells with 8.6 at.% Sn and SiGeSn barriers incorporating 10.9/10.5 at.% Sn/Si, respectively, as determined by APT (not shown here). The thickness of the active layers was around 19 nm, while the SiGeSn barriers were roughly 11 nm thick. A 50 nm p-type doped GeSn layer on top, with an active hole concentration of 7E18 cm^{-3}, completes the structure. The main benefit of SiGeSn introduction can be seen from the band alignment calculations in Figure 6 (b). Despite the increased Sn content in the barrier, the incorporation of Si atoms leads distinct band energy shifts, yielding a type I alignment, advantageous for carrier confinement in the active region. It should be noted that the chosen bowing parameter of $b^{SiSn} = 19.2\ eV$ again overestimates the

directness of the SiGeSn alloy (cf. our previous results), thus, it probably underestimates the real carrier confinement.

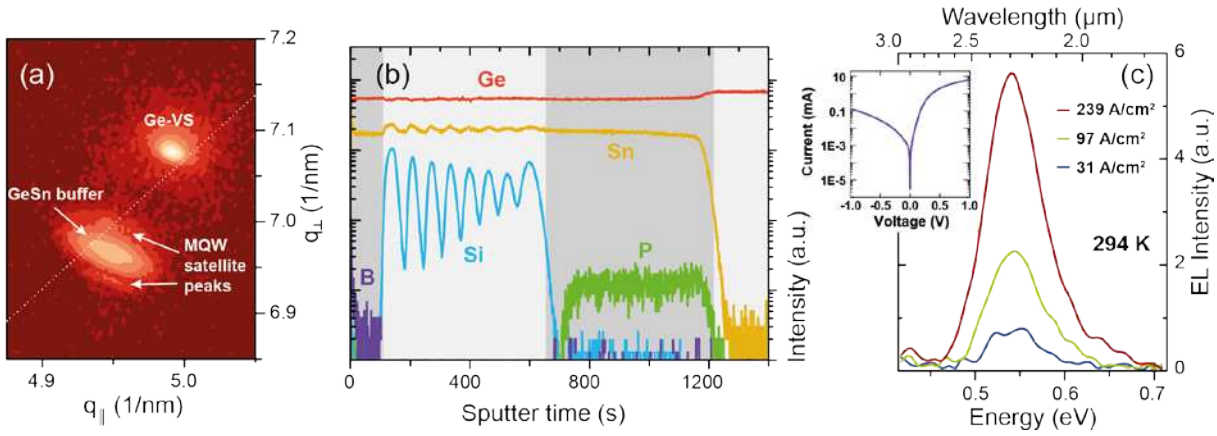

Figure 7. *(a): XRD-RSM of the grown structure demonstrates wells grown coherently on the GeSn buffer. (b): SIMS depth profiling clearly shows the MQW structure and doped claddings. (c): Room temperature electroluminescence of a fabricated 100 µm diameter LED and diode-like I-V characteristic (inset).*

In **Figure 7**(a) the reciprocal space map of the grown heterostructure is shown. A clear peak can be assigned to the GeSn buffer, showing partial layer relaxation, as desired. The buffer peak is surrounded by satellite peaks from the GeSn/SiGeSn MQW, however, only the first order peaks can be distinguished. This may be caused by the non-ideal periodicity of the MQW, which can better be seen in secondary ion mass spectrometry (SIMS), depicted in Figure 7(b). Herein, the MQW is resolved by the oscillation in Si content. The higher Sn content in the barrier region is a consequence of a non-optimized growth scheme. Feeding disilane into the reactor during GeSn epitaxy, while leaving all other growth parameters constant, leads, in addition to Si incorporation, to a slight increase of the Sn content[24]. This effect has to be taken into account in more complex growth schemes for future CVD-grown heterostructures to improve carrier confinement in the device. Another important feature, which can be seen from the SIMS depth profiling, is the in-situ doping of the p- and n-type doped hole and electron injection layers. To keep the dopants away from the active layer, and thus, reduce additional

free carrier absorption, in-situ doping of the bottom contact was stopped approximately 60 nm below the first barrier. Furthermore, the MQW is designed in such way that the outer barriers, enclosing the active region, exhibit slightly higher thicknesses of about 21 nm. Hence, the grown heterostructure features all the required building blocks for an efficient group IV light emitting device.

To prove its suitability for light emission, circular LEDs were fabricated, following the process flow from reference[19]. The current-voltage characteristics, provided in the inset of Figure 7(c), depict a diode like behavior of the device with distinct forward- and reverse-bias regimes. As shown in Figure 7(c), strong room temperature electroluminescence at around 2.3 µm (539 meV) is detected for current densities as low as 31 A cm^{-2}, comparable to state-of-the-art GeSn-based light emitting diodes[18,19]. Light emission is strongly increased in comparison to similar MQW devices with Ge barriers[19], which we attribute to an improved carrier confinement, highlighting the potential of using SiGeSn in heterostructure light emitters. Extensive further optical characterization and analysis of the MQW devices are reported elsewhere[40].

3. Conclusion

In this contribution, we discussed the epitaxy of SiGeSn ternaries tailored for optoelectronic applications. The interplay between growth temperature and cracking efficiency of different precursors enables epitaxy of a broad range of stoichiometries, with Si and Sn concentrations up to 15 at.%. Furthermore, we inquired the relaxation behavior in ternaries to substantiate the interest of their use as SRBs in heterostructure devices. Temperature-dependent photoluminescence experiments indicate efficient light emission below 2.3 µm and hint at a compositional-dependent direct gap bowing parameter b^{SiSn}. Impact of stoichiometry on band structure was shown by means of reflection measurements. Absorption edges up to 2.5 µm promise a wide range of optoelectronic applications in the short-wave infrared spectrum. We exemplified this by growth of a GeSn/SiGeSn MQW heterostructure with important device modules such as in-situ doping and cladding layers. Strong room temperature light emission at

around 2.3 µm experimentally proves the potential of integrating SiGeSn for highly efficient group IV light emitters.

4. Experimental Section

Thin Film Deposition:

The investigated SiGeSn layers were grown on 200 mm wafers using reactive gas source epitaxy in an industry-compatible reactor with showerhead gas delivery design, which assures a homogeneous precursor distribution on top of the wafer. To minimize the large lattice mismatch between Si, Ge and α-Sn, growth is performed on top of 2.5 µm thick, cyclically annealed Ge virtual substrates (Ge-VS), which were produced beforehand in another reactor on standard Si(100) wafers[41]. Commercially available low temperature cracking precursor gases, as disilane (Si_2H_6), digermane (Ge_2H_6) and tin tetrachloride ($SnCl_4$), ensure high growth rates of about 10 nm min^{-1} at temperatures as low as 340°C, mandatory for suppressing quality degradation by Sn surface segregation and bulk precipitates. Additionally, the liquid $SnCl_4$ precursor requires the use of a bubbler source for vaporization before injecting it into the gas mixing system.

To form carrier injection layers in GeSn/SiGeSn heterostructures, in-situ doping of the cladding layers using gaseous phosphine (PH_3) and diborane (B_2H_6) was performed, to avoid ion implantation-induced damage. All gases are supplied into the chamber using nitrogen as carrier gas, leading to a total gas flow of only a few standard liter per minute (slm). Prior to growth, the native oxide is removed ex-situ in a fully automated single-wafer cleaning tool based on HF vapor chemistry. Additionally, an in-situ hydrogen bake is performed at a temperature of about 850°C, ensuring a contaminant-free wafer surface fit for epitaxy.

Layer characterization:

Layer thickness, stoichiometry and crystalline quality were extracted from RBS measurements using 1.4 MeV He^+ ions, while the data were analyzed by the RUMP simulation software.

Comparing channeling measurements, performed on samples aligned along the (001) crystallographic direction with arbitrarily aligned (random) RBS measurements, allows determination of the minimum channeling yield, χ_{min}. This ratio between channeling and random spectra, taken directly behind the surface peak, is a measure of the substitutionality in the alloy and thus provides information on the layer's crystalline quality. The latter, as well as the overall layer morphology are further investigated by XTEM, using a Tecnai G2 TF20 S-TWIN system.

Tetragonal lattice distortions by biaxial tensile or compressive strain sensitively influence the electronic band structure of the alloy. These deviations from the cubic crystal lattice are evaluated by X-ray diffraction reciprocal space mapping (XRD-RSM) around the asymmetric (224) reflection, employing a Bruker D8 high-resolution diffractometer and the K_α line of Cu (1.54 Å).

The absorption properties of the grown ternaries were investigated in a Bruker VERTEX 80 V FTIR spectrometer system. Halogen and Globar SiC lamps were used as near- and mid-infrared light sources, respectively, while absorption spectra were acquired by a liquid nitrogen cooled HgCdTe detector. For optimal light collection, the samples were positioned inside an integrating sphere on a reflecting sample holder, both coated with gold.

Temperature dependent photoluminescence measurements were performed using a continuous-wave solid-state laser with an excitation wavelength of 532 nm and an output power of about 2 mW. Emitted PL was detected by a nitrogen-cooled InSb detector, offering a detection range as low as 0.27 eV. The same detector type was also used for collecting electroluminescence (EL) of fabricated LEDs, which were excited by a voltage source with a repetition rate of ~2 kHz and a duty cycle of 50 %.

Acknowledgements

This research received funding for CVD growth investigations from Federal Ministry of Education and Research (BMBF) under project *UltraLowPow* (16ES0060 K). We acknowledge support by the German Research Foundation (DFG) through the project *SiGeSn*

Laser for Silicon Photonics. We thank Steffi Lenk for her assistance with TEM measurements.
S.W. is now with IBM Research – Zurich, 8803 Rueschlikon, Switzerland.
R.G. is now with Intel Mobile Communications GmbH – Munich, 85579 Neubiberg, Germany

Received: ((will be filled in by the editorial staff))
Revised: ((will be filled in by the editorial staff))
Published online: ((will be filled in by the editorial staff))

[1] R. Soref, *Nat. Photonics* **2010**, *4*, 495.

[2] R. Soref, D. Buca, S.-Q. Yu, *Opt. Photonics News* **2016**, 32.

[3] J. J. Ackert, D. J. Thomson, L. Shen, A. C. Peacock, P. E. Jessop, G. T. Reed, G. Z. Mashanovich, A. P. Knights, *Nat. Photonics* **2015**, *9*, 393.

[4] Z. Liu, Y. Chen, Z. Li, B. Kelly, R. Phelan, J. O'Carroll, T. Bradley, J. P. Wooler, N. V Wheeler, A. M. Heidt, T. Richter, C. Schubert, M. Becker, F. Poletti, M. N. Petrovich, S. Alam, D. J. Richardson, R. Slav'ik, *J. Light. Technol.* **2015**, *33*, 1373.

[5] G. T. Reed, G. Mashanovich, F. Y. Gardes, D. J. Thomson, *Nat. Photonics* **2010**, *4*, 518.

[6] C. Sun, M. T. Wade, Y. Lee, J. S. Orcutt, L. Alloatti, M. S. Georgas, A. S. Waterman, J. M. Shainline, R. R. Avizienis, S. Lin, B. R. Moss, R. Kumar, F. Pavanello, A. H. Atabaki, H. M. Cook, A. J. Ou, J. C. Leu, Y.-H. Chen, K. Asanović, R. J. Ram, M. A. Popović, V. M. Stojanović, *Nature* **2015**, *528*, 534.

[7] Z. Wang, B. Tian, M. Pantouvaki, W. Guo, P. Absil, J. Van Campenhout, C. Merckling, D. Van Thourhout, *Nat. Photonics* **2015**, *9*, 837.

[8] S. Chen, W. Li, J. Wu, Q. Jiang, M. Tang, S. Shutts, S. N. Elliott, A. Sobiesierski, A. J. Seeds, I. Ross, P. M. Smowton, H. Liu, *Nat. Photonics* **2016**, 1.

[9] S. Gupta, B. Magyari-Köpe, Y. Nishi, K. C. Saraswat, *J. Appl. Phys.* **2013**, *113*, 073707.

[10] K. Lu Low, Y. Yang, G. Han, W. Fan, Y.-C. Yeo, *J. Appl. Phys.* **2012**, *112*, 103715.

[11] C. Eckhardt, K. Hummer, G. Kresse, *Phys. Rev. B* **2014**, *89*, 165201.

[12] N. von den Driesch, D. Stange, S. Wirths, G. Mussler, B. Holländer, Z. Ikonic, J. M. Hartmann, T. Stoica, S. Mantl, D. Grützmacher, D. Buca, *Chem. Mater.* **2015**, *27*, 4693.

[13] S. A. Ghetmiri, W. Du, J. Margetis, A. Mosleh, L. Cousar, B. R. Conley, L. Domulevicz, A. Nazzal, G. Sun, R. A. Soref, J. Tolle, B. Li, H. A. Naseem, S.-Q. Yu, *Appl. Phys. Lett.* **2014**, *105*, 151109.

[14] C. L. Senaratne, J. D. Gallagher, T. Aoki, J. Kouvetakis, J. Menéndez, *Chem. Mater.* **2014**, *26*, 6033.

[15] D. Stange, S. Wirths, N. von den Driesch, G. Mussler, T. Stoica, Z. Ikonic, J. M. Hartmann, S. Mantl, D. Grützmacher, D. Buca, *ACS Photonics* **2015**, *2*, 1539.

[16] S. Wirths, R. Geiger, N. von den Driesch, G. Mussler, T. Stoica, S. Mantl, Z. Ikonic, M. Luysberg, S. Chiussi, J. M. Hartmann, H. Sigg, J. Faist, D. Buca, D. Grützmacher, *Nat. Photonics* **2015**, *9*, 88.

[17] S. Al-Kabi, S. A. Ghetmiri, J. Margetis, T. Pham, Y. Zhou, W. Dou, B. Collier, R. Quinde, W. Du, A. Mosleh, J. Liu, G. Sun, R. A. Soref, J. Tolle, B. Li, M. Mortazavi, H. A. Naseem, S.-Q. Yu, *Appl. Phys. Lett.* **2016**, *109*, 171105.

[18] W. Du, Y. Zhou, S. A. Ghetmiri, A. Mosleh, B. R. Conley, A. Nazzal, R. A. Soref, G. Sun, J. Tolle, J. Margetis, H. A. Naseem, S.-Q. Yu, *Appl. Phys. Lett.* **2014**, *104*, 241110.

[19] D. Stange, N. von den Driesch, D. Rainko, C. Schulte-Braucks, S. Wirths, G. Mussler, A. T. Tiedemann, T. Stoica, J. M. Hartmann, Z. Ikonic, S. Mantl, D. Grützmacher, D. Buca, *Opt. Express* **2016**, *24*, 1358.

[20] G. Sun, R. A. Soref, H. H. Cheng, *Opt. Express* **2010**, *18*, 19957.

[21] A. Attiaoui, O. Moutanabbir, *J. Appl. Phys.* **2014**, *116*, 063712.

[22] P. Moontragoon, R. A. Soref, Z. Ikonic, *J. Appl. Phys.* **2012**, *112*, 073106.

[23] J. D. Gallagher, C. Xu, C. L. Senaratne, T. Aoki, P. M. Wallace, J. Kouvetakis, J. Menéndez, *J. Appl. Phys.* **2015**, *118*, 135701.

[24] S. Wirths, D. Buca, Z. Ikonic, P. Harrison, A. T. Tiedemann, B. Holländer, T. Stoica, G. Mussler, U. Breuer, J. M. Hartmann, D. Grützmacher, S. Mantl, *Thin Solid Films* **2014**, *557*, 183.

[25] T. Yamaha, O. Nakatsuka, S. Takeuchi, W. Takeuchi, N. Taoka, K. Araki, K. Izunome, S. Zaima, *ECS Trans.* **2013**, *50*, 907.

[26] S. Wirths, A. T. Tiedemann, Z. Ikonic, P. Harrison, B. Holländer, T. Stoica, G. Mussler, M. Myronov, J. M. Hartmann, D. Grützmacher, D. Buca, S. Mantl, *Appl. Phys. Lett.* **2013**, *102*, 192103.

[27] I. A. Fischer, T. Wendav, L. Augel, S. Jitpakdeebodin, F. Oliveira, A. Benedetti, S. Stefanov, S. Chiussi, G. Capellini, K. Busch, J. Schulze, *Opt. Express* **2015**, *23*, 25048.

[28] R. T. Beeler, D. J. Smith, J. Kouvetakis, J. Menéndez, *IEEE J. Photovoltaics* **2012**, *2*, 434.

[29] C. D. Thurmond, F. A. Trumbore, M. Kowalchik, *J. Chem. Phys.* **1956**, *25*, 799.

[30] R. Chen, Y.-C. Huang, S. Gupta, A. C. Lin, E. Sanchez, Y. Kim, K. C. Saraswat, T. I. Kamins, J. S. Harris, *J. Cryst. Growth* **2013**, *365*, 29.

[31] L. Jiang, C. Xu, J. D. Gallagher, R. Favaro, T. Aoki, J. Menéndez, J. Kouvetakis, *Chem. Mater.* **2014**, *26*, 2522.

[32] V. R. D'Costa, Y. Y. Fang, J. Tolle, J. Kouvetakis, J. Menéndez, *Phys. Rev. Lett.* **2009**, *102*, 1.

[33] T. Wendav, I. A. Fischer, M. Montanari, M. H. Zoellner, W. Klesse, G. Capellini, N. von den Driesch, M. Oehme, D. Buca, K. Busch, J. Schulze, *Appl. Phys. Lett.* **2016**, *108*, 242104.

[34] E. Kasper, J. Werner, M. Oehme, S. Escoubas, N. Burle, J. Schulze, *Thin Solid Films* **2012**, *520*, 3195.

[35] M. J. Almond, A. M. Doncaster, P. N. Noble, R. Walsh, *J. Am. Chem. Soc.* **1982**, *104*, 4717.

[36] S. Gupta, E. Simoen, H. Vrielinck, C. Merckling, B. Vincent, F. Gencarelli, R. Loo, M. Heyns, *ECS Trans.* **2013**, *53*, 251.

[37] V. R. D'Costa, C. S. Cook, A. G. Birdwell, C. L. Littler, M. Canonico, S. Zollner, J. Kouvetakis, J. Menéndez, *Phys. Rev. B* **2006**, *73*, 125207.

[38] P. G. Moses, C. G. Van de Walle, *Appl. Phys. Lett.* **2010**, *96*, 021908.

[39] A. Belabbes, M. Ferhat, A. Zaoui, *Appl. Phys. Lett.* **2006**, *88*, 0.

[40] D. Stange, N. von den Driesch, D. Rainko, S. Roesgaard, I. Povstugar, J.-M. Hartmann, T. Stoica, Z. Ikonić, S. Mantl, D. Grützmacher, D. Buca, *Optica* **2016**, *in press*.

[41] J. M. Hartmann, A. Abbadie, N. Cherkashin, H. Grampeix, L. Clavelier, *Semicond. Sci. Technol.* **2009**, *24*, 055002.